

Linköping Studies in Science and Technology
Licentiate Thesis No. 2035

Sn- and Bi-Based Catalysts for CO₂ Electroreduction

Yuguo Zhao

Linköping Studies in Science and Technology. Licentiate Thesis No. 2035

Sn- and Bi-Based Catalysts for CO₂ Electroreduction

Yuguo Zhao



Division of Nanostructured Materials
Department of Physics, Chemistry and Biology (IFM),
Faculty of Science and Engineering
Linköpings universitet, SE-581 83 Linköping, Sweden
Linköping 2026

Supervisor:

Emma Björk

Professor

Nanostructured Materials, IFM

Co-supervisor:

Magnus Odén

Professor

Nanostructured Materials, IFM


Faculty opponent:

Mathilde Luneau

Assistant Professor

Applied Chemistry, Chalmers University of Technology

© Yuguo Zhao, 2026

 Except where otherwise noted, this work is licensed under a Creative Commons Attribution 4.0 International license. To view a copy of this license, visit:

<https://creativecommons.org/licenses/by/4.0/>

Printed in Sweden by LiU-tryck, 2026

ISBN 978-91-8118-589-8 (print)

ISBN 978-91-8118-648-2 (PDF)

<https://doi.org/10.3384/9789181186482>

ISSN 0280-7971

Abstract

Electrocatalytic CO₂ reduction to formate/formic acid represents a practical and economically viable route for CO₂ conversion, among which Sn- and Bi-based materials are regarded as promising electrocatalysts. This thesis explores the structure–performance relationship of Sn- and Bi-based catalysts for electrochemical CO₂ reduction reaction (CO₂RR) to formate, focusing on two effective optimization strategies: mesostructural engineering and heterometal doping. Sn- and Bi-based catalysts are attractive candidates due to their high selectivity for formate, low cost, and environmental compatibility.

In the first study, mesoporous SnO₂ enriched with oxygen vacancies shows enhanced CO₂RR performance compared with bulk SnO₂ and improved durability. Mechanistic studies reveal that the mesostructure enhances CO₂ adsorption, facilitates charge transfer, stabilizes the *OCHO intermediate, and lowers the reaction energy barrier. Moreover, the mesoporous framework promotes the formation and stabilization of oxygen vacancies, maintaining the Sn oxidation state and catalyst stability.

In the second study, Sn-doped BiOCl (the ratio of Sn is 2-10 at. %) nanoplates synthesized via a sol–gel method act as precatalysts that rapidly reconstruct into Sn-modified metallic Bi during the CO₂RR. Among the samples investigated, the catalyst with a Sn doping ratio of ~5% achieves a Faradaic efficiency of 87.7% at –1.0 V vs. RHE, considerably outperforming pristine BiOCl. Structural and spectroscopic analyses show that Sn incorporation stabilizes the *OCHO intermediate, facilitates interfacial water dissociation, and promotes the formation of active Bi 003 planes, clarifying the dynamic evolution of active sites.

Overall, this thesis demonstrates that rational control of mesostructure, defect chemistry, and dopant-induced reconstruction can synergistically enhance both activity and stability in Sn- and Bi-based CO₂RR catalysts. These insights provide practical guidelines for designing efficient and durable formate-selective electrocatalysts.

Keywords: CO₂ electroreduction, electrocatalysts, formate production, performance-structure relationships

Populärvetenskaplig sammanfattning

Koldioxidutsläpp är en av de främsta orsakerna till dagens klimatförändringar. Att omvandla koldioxid (CO_2) till användbara kemikalier i stället för att släppa ut den i atmosfären är ett attraktivt angreppssätt för att minska dessa utsläpp. Elektrokemisk reduktion av CO_2 (CO_2RR) till värdefulla kemikalier och bränslen med hjälp av förnybar energi är en möjlig väg framåt. Bland de olika produkter som bildas är formiat särskilt attraktivt då den kan fungera som en kemisk råvara och en potentiell vätebärare. Formiat kan produceras elektrokemiskt från CO_2 med relativt hög hastighet och selektivitet, vilket gör metoden lämplig för storskaliga tillämpningar.

En stor utmaning inom CO_2RR är utvecklingen av effektiva elektrokatalysatorer. Katalysatorerna påskyndar reaktionen och styr vilka produkter som bildas. Idealt bör en katalysator omvandla CO_2 till formiat effektivt och samtidigt vara stabil under långvarig drift. Tidigare studier har visat att katalysatorer baserade på tenn (Sn) och vismut (Bi) är lovande kandidater för detta. De kan främja bildande av formiat samtidigt som de hämmar konkurrerande reaktioner, såsom väteutvecklingsreaktionen, som annars sänker effektiviteten i CO_2 -omvandlingen.

Mot denna bakgrund undersöker denna avhandling två katalysatorsystem baserade på Sn och Bi. För tennoxid (SnO_2) konstruerades katalysatorn med en mesoporös struktur. Detta innebär att materialet innehåller ett nätverk av mycket små porer, några nanometer breda. Dessa porer ökar materialets yta och ger fler aktiva platser där reaktionen kan ske. Materialet tillverkades med syrevakanser, det vill säga avsaknad av några syreatomer i kristallstrukturen. Dessa vakanser gör ytan mer katalytiskt aktiv, förbättrar adsorptionen av CO_2 och hjälper till att stabilisera viktiga

reaktionsintermediärer under den katalytiska processen. Denna katalysator uppvisar högre aktivitet och bättre långtidsstabilitet än konventionell SnO₂.

Det andra systemet är baserat på vismutoxyklorid (BiOCl). När små mängder Sn införs i detta material genomgår katalysatorn en strukturell omvandling, rekonstruktion, under reaktionen och bildar en Sn-modifierad metallisk Bi-yta. Den rekonstruerade yta exponerar särskilt aktiva kristallplan och underlättar viktiga reaktionssteg, såsom bildningen av centrala intermediärer och aktiveringen av vattenmolekyler. Som ett resultat producerar katalysatorn formiat mycket mer selektivt än ren BiOCl utan Sn.

Sammantaget visar resultaten i den här avhandlingen att kontroll av porstruktur, atomära vakanser och dopnings-inducerad rekonstruktion effektivt kan styra aktivitet och selektivitet hos CO₂-reduktionskatalysatorer. Dessa insikter ger värdefull vägledning för utformningen av effektiva och hållbara katalysatorer för hållbar CO₂-omvandling.

Preface

This licentiate thesis is part of my PhD studies in the Nanostructured Materials Division at Department of Physics, Chemistry and Biology (IFM), Linköping University since Sept. 2023. I am also enrolled in the graduate school Agora Materiae, a multidisciplinary doctoral program at Linköping University.

This thesis is financially supported by Swedish Energy Agency (No. 2022-00909).

Some of the content of this thesis was edited using generative AI assistance to improve spelling and grammar.

Linköping, March 2026

Yuguo Zhao

Acknowledgements

This thesis could not have been completed without the support and encouragement from many wonderful people.

First and foremost, I would like to express my deepest gratitude to my main supervisor, Prof. Emma M. Björk, for her unwavering support throughout my PhD journey. Her insightful discussions, guidance, and continuous encouragement have been invaluable for both the planning and execution of my experiments since September 2023.

I am also very grateful to my co-supervisor, Prof. Magnus Odén, for his thoughtful advice and continuous support throughout the PhD studies.

My sincere thanks go to Dr. Mikhail Vagin for his generous guidance with electrochemical measurements at ITN during the early stages of this project, as well as for his valuable discussions on electrochemistry.

I would like to thank all members of the Nanostructured Materials Division for creating a collaborative and joyful working environment. I especially want to thank Valentina Guerrero Florez for her great help in the lab. I also want to thank all colleagues and friends at IFM and ITN, in Sweden and China, for their constant support and care.

I am deeply grateful to Prof. Yong Yan for his enduring support since my master's studies.

I also thank our industrial partners from SCA Forest Products (Sweden) and Noram Engineering (Canada) for their insightful discussions.

I also thank Dr. Yueshuai Wang for his help with STEM measurements, Prof. Shoushuang Huang for his help on DFT calculations, Dr. Robert Boyd for assistance with TEM, Dr. Lingyin Meng for help with centrifuge experiments, Zesheng Liu and Prof. Mats Fahlman for their assistance with XPS.

I would like to thank Caroline Brommesson for organizing the Agora Materiae Graduate School and Anna Brodzka for handling administrative and financial matters.

I gratefully acknowledge financial support from the Swedish Energy Agency.

Finally, I want to express my heartfelt gratitude to my family, and especially to my girlfriend, Mengyue Xu, for her support and for always standing by my side.

List of included papers

Paper I

Synergistic Effects of Mesoporous Structure and Oxygen Vacancies in SnO₂ for Enhanced CO₂ Electroreduction

Yuguo Zhao, Shoushuang Huang, Yong Yan, Robert Boyd, Zesheng Liu, Mats Fahlman, Mikhail Vagin, Magnus Odén, and Emma M. Björk

Small Science, 2026, 6, e70268. <https://doi.org/10.1002/smsc.70268>.

Author contribution: I carried out most of the planning and experiments. I performed the majority of the physical characterization, except for STEM, XPS, and CO₂-TPD measurements. I conducted electrochemical and in situ experiments. I carried out the primary data analysis with input from the co-authors. I wrote the manuscript and contributed to the revisions.

Paper II

Sn-Induced BiOCl Reconstruction Enhances Facet-Selective CO₂-to-formate Conversion

Yuguo Zhao, Yueshuai Wang, Yong Yan, Robert Boyd, Mikhail Vagin, Magnus Odén, and Emma M. Björk

In manuscript.

Author contribution: I was responsible for the overall planning and experiments. I performed most of the physical characterization, except for STEM, XPS, and AFM measurements. I conducted electrochemical and in situ experiments. I carried out the primary data analysis with input from the co-authors. I wrote the manuscript and contributed to the revisions before submission.

Contents

Abstract	i
Populärvetenskaplig sammanfattning	iii
Preface	v
Acknowledgements	vi
List of included papers	viii
Chapter 1: Introduction	1
1.1 Significance.....	1
1.2 Scope of this thesis.....	2
Chapter 2: Motivations and background	4
2.1 Fundamentals of CO ₂ RR	4
2.1.1 Electrochemical cells	4
2.1.2 Reaction pathways	6
2.2 Selection and optimization of catalysts	10
2.2.1 Selection of catalysts.....	11
2.2.2 Catalyst optimization	12
Chapter 3: Methodology	15
3.1 Materials synthesis and electrode preparation.....	15
3.1.1 Materials synthesis	15
3.1.2 Electrode preparation	16
3.2 Electrochemical measurements	17
3.2.1 Voltammetry	18
3.2.2 Electrochemical impedance spectroscopy.....	19
3.2.3 Chronoamperometry.....	21
3.2.4 CO ₂ RR product analysis.....	22
3.3 Physical characterization	23
3.3.1 X-ray diffraction	23
3.3.2 Electron microscopy	24
3.3.3 X-ray photoelectron spectroscopy	27
3.3.4 Physisorption.....	28
3.4 In situ characterization of CO ₂ RR	30

3.4.1 Vibrational spectroscopy	30
3.4.2 X-ray based techniques	34
Chapter 4: Summary of included papers	37
4.1 Paper I	37
4.2 Paper II	38
Chapter 5: Outlook	39
References	41

Chapter 1: Introduction

1.1 Significance

Since the industrial revolution, fossil resources, such as coal, oil, and natural gas, have been extensively exploited to sustain industrialization and economic growth. Their high energy density and versatility as fuels and chemical feedstocks have supported rapid global industrial and economic development for more than a century. However, this growth has been accompanied by the progressive depletion of finite natural resources and the large-scale emission of greenhouse gases. In 2023, atmospheric CO₂ concentrations reached approximately 151% of pre-industrial levels,¹ posing severe risks to the environment and global climate. The transition toward renewable energy sources such as wind, solar, and hydropower has become essential for sustainable development. Over the past decade, the cost of renewable electricity has declined significantly. In many regions, it is now competitive with or even lower than that of fossil-based energy.² The intermittent nature of solar and wind energy necessitates the development of efficient energy storage strategies. Converting green electricity into chemical energy provides a route for storing intermittent renewable power in the form of chemical fuels, offering higher energy density, long-term storage capability, and ease of transportation.

Beyond its role in energy systems, carbon remains an indispensable element in modern society, serving as a fundamental building block for fuels, chemicals, and materials. Currently, approximately 85% of carbon feedstocks are derived from fossil resources, about 10% from biomass, and only 5% from recycled carbon.³ The demand for carbon embedded-chemical products is projected to increase to 1 Gt annually by 2050.⁴ Meeting this growing demand while minimizing CO₂

emissions requires the establishment of a circular carbon economy. Electrochemical CO₂ reduction (CO₂RR) to value-added chemicals and fuels represents a promising route toward this goal. As illustrated in Figure 1.1, the electrochemical CO₂ conversion process utilizes renewable electricity and water as the proton source to convert CO₂ into chemical products suitable for storage and distribution. CO₂RR can also be conducted under mild and controllable conditions, such as ambient temperature and pressure, suggesting its potential feasibility for practical implementation.

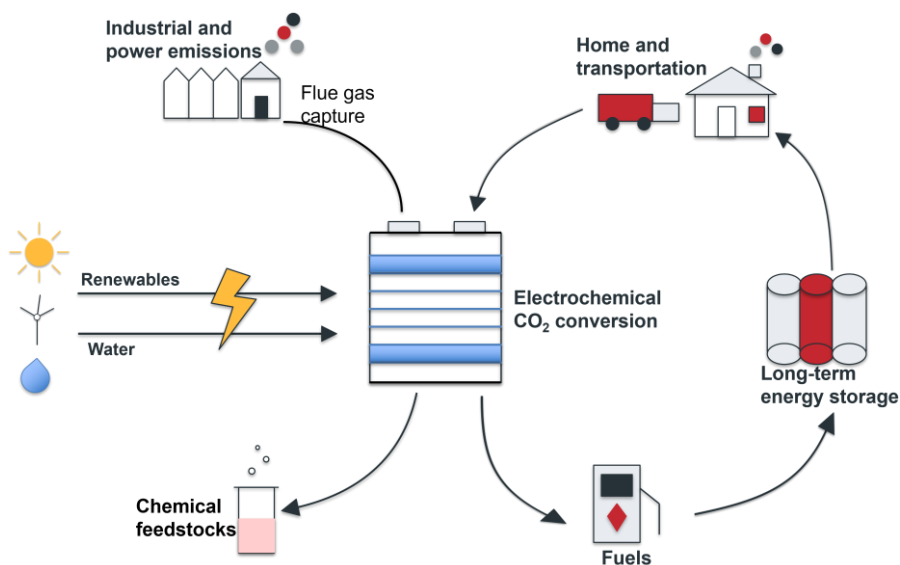


Figure 1.1 Concept of electrochemical CO₂ conversion using renewable energy and waste CO₂ emissions as carbon sources.

1.2 Scope of this thesis

The general objective of this thesis is to advance efficient formate production via electrochemical CO₂RR. Formate is widely regarded as a valuable chemical feedstock and a potential hydrogen energy carrier. Achieving high selectivity and stability in CO₂RR critically depends on the rational design of electrocatalysts. Therefore, this work focuses on elucidating structure–performance relationships of Sn- and Bi-

based catalysts to guide the development of efficient electrocatalysts for CO₂-to-formate conversion.

Specifically, this thesis aims to:

- understand the effects of pore structure and oxygen vacancies on the CO₂ electroreduction performance of metal oxide catalysts, and
- gain insight into how heterometal doping influences the catalytic behaviour of metal oxide catalysts toward CO₂ reduction.

In summary, the goal is to establish a clearer link between structural/compositional modification and improvements in the catalyst activity and selectivity. The findings could provide design guidelines for developing more efficient oxide-based electrocatalysts

Chapter 2: Motivations and background

2.1 Fundamentals of CO₂RR

The electrochemical CO₂RR process is influenced by several factors, including the type of electrochemical cell, electrocatalyst, and operating conditions such as pressure and temperature.⁵⁻⁷ This section discusses these key factors from the perspectives of electrochemical cell design, reaction pathways, and catalyst design and optimization strategies.

2.1.1 Electrochemical cells

Three main types of electrochemical cells are used for CO₂RR. Most fundamental studies have been conducted in an H-type cell (Figure 2.1(a)). This configuration typically uses a three-electrode setup, in which the working electrode (cathode) and reference electrode are placed in the cathodic compartment, while the counter electrode (anode) is in a separate anodic compartment. The two chambers are separated by an ion-exchange membrane to prevent product crossover while maintaining ionic conductivity. The H-cell provides a well-controlled platform that is widely used for mechanistic investigations.⁸ However, the low solubility and diffusivity of CO₂ in aqueous electrolytes impose intrinsic mass transport limitations, resulting in low current densities.⁹ The relatively large inter-electrode distance leads to increased ohmic resistance, further constraining overall cell performance.^{9, 10} These limitations restrict H-cell configurations to laboratory-scale catalyst evaluation, making it difficult to achieve the high current densities required for practical applications.

To address these limitations, flow-cell configurations have been developed. In a typical flow cell (Figure 2.1(b)), porous hydrophobic gas diffusion electrodes (GDEs) are used together with an ion-

exchange membrane that separates the cathodic and anodic compartments. CO₂ is supplied directly to the GDE, where CO₂RR occurs at a gas–liquid–solid three-phase interface. This configuration substantially improves mass transport.¹¹ The reduced distance between the anode and cathode also reduces internal resistance, allowing operation at higher current densities.¹⁰ Nevertheless, flow cells are prone to electrolyte flooding, where loss of GDE hydrophobicity permits electrolyte penetration into the gas diffusion layer, blocking CO₂ transport pathways and suppressing the three-phase interface, leading to performance decay.¹²

Membrane electrode assembly (MEA) systems were developed to overcome the mass transport limitations and flooding issues associated with the conventional flow cell configurations (Figure 2.1(c)). In an MEA configuration, no liquid catholyte flows through the cathodic chamber; instead, humidified CO₂ is delivered through the GDE, and the reaction proceeds predominantly at the gas–solid interface, thereby minimizing flooding and enabling stable operation at industrially relevant current densities.⁷

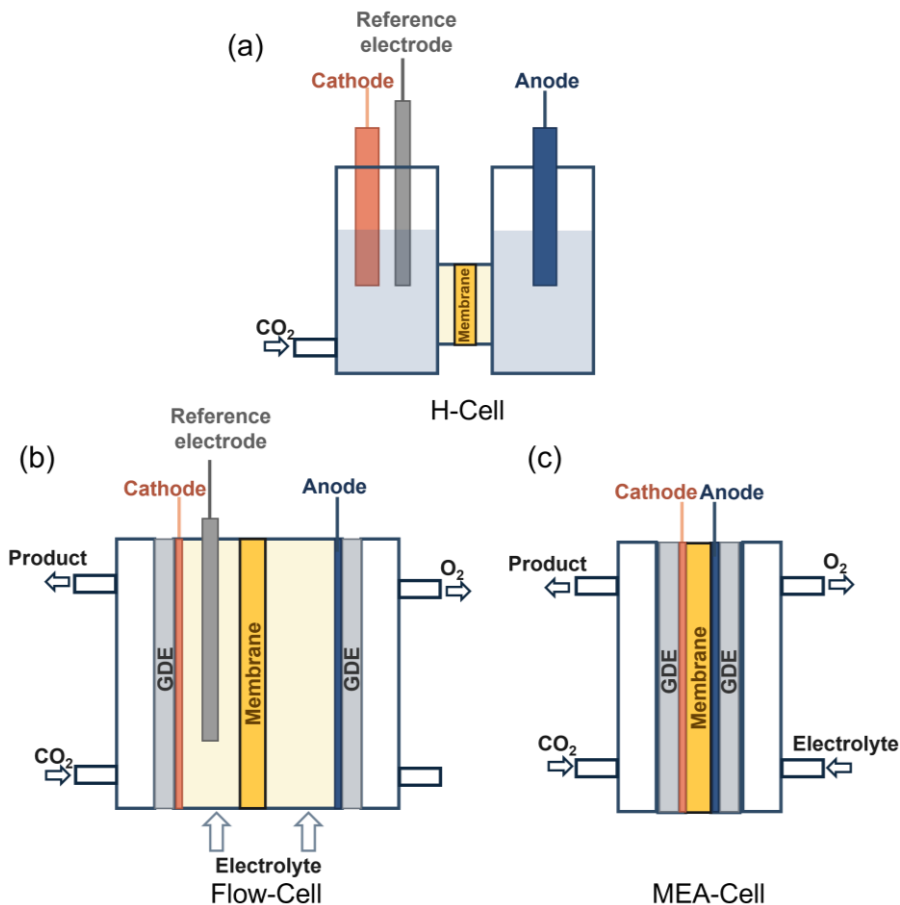


Figure 2.1 Schematic configurations of electrochemical cells employed for CO₂RR: (a) H-cell, (b) flow cell, and (c) membrane electrode assembly (MEA).

2.1.2 Reaction pathways

In a typical electrochemical CO₂RR system (Figure 2.2), water oxidation takes place at the anode, while CO₂ reduction occurs at the cathode, accompanied by the competing hydrogen evolution reaction (HER). Depending on the electrocatalyst employed, CO₂ can be converted into a variety of products. These include C₁ products, such as carbon monoxide (CO) and formic acid (HCOOH), as well as C₂+

products, including ethanol (C_2H_5OH) and ethylene (C_2H_4). Some CO_2 reduction pathways involve the transfer of up to 18 electrons per molecule. The half-reactions for CO_2 reduction and the competing HER, together with their standard potentials (vs. SHE at pH 7.0), are summarized in Table 2.1.¹³

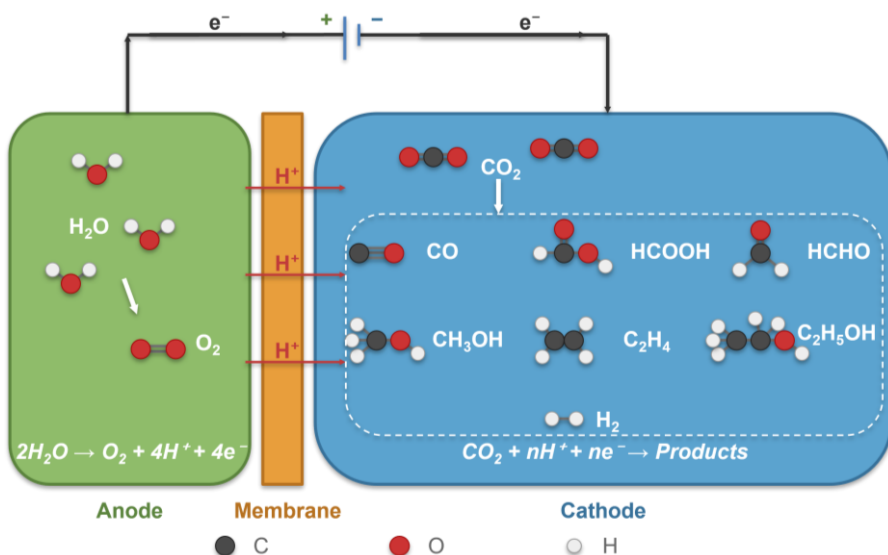


Figure 2.2 Schematic illustration of a CO_2RR electrolyzer: CO_2 is reduced to value-added products in the cathodic chamber, while the oxygen evolution reaction (OER) takes place in the anodic chamber.

Table 2.1 Standard potentials of possible CO₂RR process and competing HER.

Products	Possible half reactions at the cathodic side	E ⁰
CO	$\text{CO}_2 + \text{H}_2\text{O} + 2\text{e}^- \rightarrow \text{CO} + 2\text{OH}^-$	-0.52
HCOO ⁻	$\text{CO}_2 + \text{H}_2\text{O} + 2\text{e}^- \rightarrow \text{HCOO}^- + 2\text{OH}^-$	-0.43
CH ₃ OH	$\text{CO}_2 + 5\text{H}_2\text{O} + 6\text{e}^- \rightarrow \text{CH}_3\text{OH} + 6\text{OH}^-$	-0.39
CH ₄	$\text{CO}_2 + 6\text{H}_2\text{O} + 8\text{e}^- \rightarrow \text{CH}_4 + 8\text{OH}^-$	-0.25
C ₂ H ₄	$2\text{CO}_2 + 8\text{H}_2\text{O} + 12\text{e}^- \rightarrow \text{C}_2\text{H}_4 + 12\text{OH}^-$	-0.34
C ₂ H ₅ OH	$2\text{CO}_2 + 9\text{H}_2\text{O} + 12\text{e}^- \rightarrow \text{C}_2\text{H}_5\text{OH} + 12\text{OH}^-$	-0.33
C ₃ H ₇ OH	$3\text{CO}_2 + 13\text{H}_2\text{O} + 18\text{e}^- \rightarrow \text{C}_3\text{H}_7\text{OH} + 18\text{OH}^-$	-0.32
H ₂	$2\text{H}_2\text{O} + 2\text{e}^- \rightarrow \text{H}_2 + 2\text{OH}^-$	-0.41

Focusing on the reaction mechanism, CO₂RR occurs through a series of proton-coupled electron transfer (PCET) steps that form various carbon-containing intermediates (Figure 2.3). Under cathodic polarization, CO₂ first absorbs on the catalyst surface. It then undergoes successive electron and proton transfers, generating intermediates such as *COOH, *OCHO, *CO, and CHO.^{14, 15} These species subsequently evolve into different products depending on how they are stabilized on the catalyst surface. For instance, *COOH is generally associated with the formation of CO, whereas *OCHO is favorable for formic acid production.¹⁶ The formation and further transformation of these intermediates are affected by factors like catalyst composition and structure, electrolyte pH, and the types of cations and anions.¹⁷ As a result, achieving high selectivity toward a specific product remains challenging. According to the Sabatier principle, selectivity depends on the adsorption strength of key intermediates. Only intermediates with optimal binding energies can efficiently convert to desired products.¹⁸

CO₂RR involves three main stages: (i) adsorption and activation of CO₂ on the catalyst surface; (ii) sequential PCET steps accompanied

by C–O bond cleavage and/or C–H bond formation; and (iii) desorption of the final products.¹⁹ The formation of C₁ products (e.g., CO, HCOOH, CH₄, and CH₃OH) typically requires fewer PCET steps and proceeds via relatively simpler pathways. In contrast, the production of C₂₊ products (e.g., C₂H₄, C₂H₅OH, CH₃COOH, C₃H₆, and n-C₃H₇OH) involves more complex reaction networks, including C–C coupling steps with high energy barriers and sluggish kinetics, which significantly limit their efficiency. Among the possible products, formic acid or formate exhibits a relatively favorable thermodynamic profile and can be produced with high selectivity on suitable catalysts. Formate or formic acid also have wide industrial applications in pharmaceuticals, metallurgy, and leather processing. Recent techno-economic analyses further suggest that targeting formic acid or CO is more practical for large-scale implementation compared to C₂₊ products, due to their higher selectivity and production rates. For these reasons, this thesis focuses on the electrocatalytic CO₂ reduction to formate.

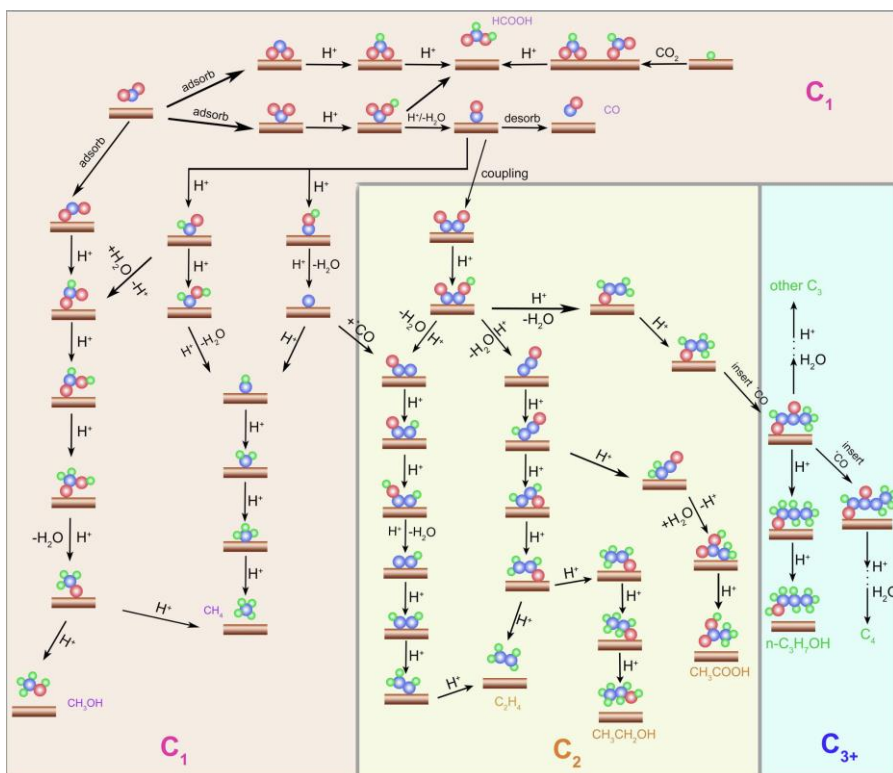


Figure 2.3 Overview of the proposed reaction pathways for CO₂RR toward various products. Reproduced from Ref. ²⁰.

2.2 Selection and optimization of catalysts

As discussed above, the product distribution in the CO₂RR process is influenced by multiple factors. Among them, the intrinsic properties of the catalyst are particularly important. The electronic structure, surface composition, and morphology of a catalyst determine the adsorption strength of key intermediates, thereby influencing the reaction pathways and product selectivity.²¹ For this reason, establishing clear structure–performance relationship is essential for the rational design and optimization of CO₂RR catalysts.

At present, CO₂RR catalysts can generally be divided into three categories: metallic catalysts, non-metallic catalysts, and molecular

catalysts.²² Each category exhibits distinct advantages and limitations with respect to activity, selectivity, and stability. This thesis focuses on the metallic catalysts to comprehensively investigate their structure–performance correlations.

From a thermodynamic standpoint, the standard reduction potentials of CO₂RR are close to those of the HER, as summarized in Table 2.1. In practice, CO₂RR typically proceeds at overpotentials much higher than the corresponding standard potential due to kinetic limitations associated with multi-electron and PCET steps. Under these conditions, HER competes with CO₂RR. Thus, developing catalysts with high selectivity toward CO₂RR, especially at large overpotentials, is important for efficient and controlled product formation.

2.2.1 Selection of catalysts

P-block metals, also known as post-transition metals, are characterized by valence electrons occupying the outermost p orbitals (ns^2np^1 – ns^2np^3 , Figure 2.4(a)). Compared to early transition metals, they generally possess relatively high electronegativity and moderate ionization energies, enabling them to adopt multiple oxidation states and form compounds with diverse valence configurations.²³ These electronic characteristics provide flexibility in activity and are advantageous for electrocatalytic applications.

For electrochemical CO₂RR to formate, post-transition metals have shown distinct advantages. As presented in Figure 2.4(b), Sn, In, Bi, and Pb have been widely reported to exhibit high selectivity toward formate or formic acid.²⁴ This behavior is commonly attributed to their favorable interaction with the *OCHO intermediate, which promotes the two-electron reduction pathway toward formate while suppressing the competing hydrogen evolution reaction (HER).²⁵

Among these metals, Sn and Bi have attracted particular attention. In comparison with Pb, they are less toxic and more environmentally acceptable,²⁶ and they are more abundant and cheaper than In.²⁴ Meanwhile, Sn and Bi oxide phases are considered to be highly active for CO₂RR to formate.²⁷ Theoretical studies have shown that the oxide surfaces with oxygen vacancies or hydroxyls provides lower kinetic barriers for CO₂ adsorption and conversion.^{28, 29} Taking these considerations together with their established catalytic performance of CO₂RR, Sn- and Bi-based materials are promising candidates for selective formate production. Based on this rationale, this thesis focuses on the design and investigation of Sn- and Bi-based catalysts for CO₂RR toward formate production.

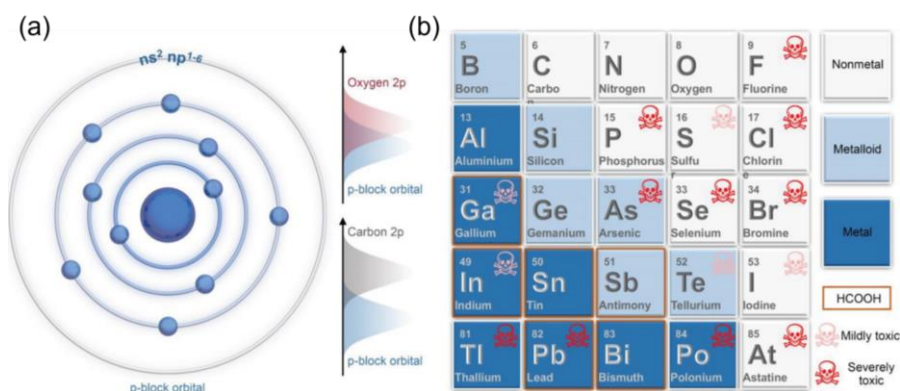


Figure 2.4 (a) Characteristics of p-block metals for CO₂RR to formate. (b) P-block elements and classification. Reproduced from Ref. ²³.

2.2.2 Catalyst optimization

In the case of conventional catalysts such as pure SnO₂ and Bi₂O₃, they are usually suffering from limited CO₂RR activity and relatively poor stability.^{30, 31} This limitation necessitates the optimization of their electronic and structural properties.

Based on this context, several strategies have been developed. One representative approach is heterometallic doping. Compared to

monometallic catalysts, bimetallic catalysts exhibit distinct properties due to their altered electronic structures.²⁶ Sun *et al.*³² reported a Cu₁-SnO₂ catalyst that outperformed pure SnO₂ in formate production. The results showed that the incorporation of Cu enhanced CO₂ adsorption and activation while stabilizing the key *OCHO intermediate. Additionally, Cu doping helped preserve the Sn-O species, thereby improving the durability of the catalyst. Similar conclusions were reported by Zhang *et al.*³³, who prepared La-doped SnO₂ and observed enhanced catalytic performance.

Beyond compositional modifications, tuning the intrinsic structural properties of catalysts has also proven effective. Facet engineering is a typical example. Luo *et al.*³⁴ showed that SnO₂ nanocubes with a high 001/110 facet ratio outperformed nanorods with lower exposure of the 001 facet. Dynamic facet evolution during electrochemical reconstruction has also been studied, particularly for Bi-based catalysts. Van der Stam *et al.*³⁵ demonstrated that halide species can regulate selective facet exposure in activated Bi-based electrocatalysts under CO₂RR conditions, leading to changes in CO₂RR selectivity.

Introducing mesoporosity has also attracted increasing attention.^{36, 37} Although mesoporous structures are commonly associated with improved mass transport, growing evidence suggests that their influence extends beyond diffusion enhancement and can markedly affect product selectivity.^{38, 39} Moreover, mesostructure formation is often accompanied by changes in surface defect chemistry, as evidenced by Al-Mayouf *et al.*³⁹ Various methods have been developed to construct mesoporous metal oxides, including soft-templating^{40, 41}, hard-templating^{42, 43}, and anodization^{44, 45}. Among these, soft-templating methods are widely explored due to their versatility in controlling pore size, morphology, and framework composition through cooperative assembly between inorganic precursors and structure-directing agents.⁴¹ Mesoporous materials can

possess either intraparticle or interparticle porosity. In interparticle systems, small primary particles assemble into interconnected networks or chain-like structures. Accumulating evidence suggests that the role of pore architecture extends beyond mass transport. Porosity-associated characteristics, including surface defects, variations in metal oxidation states, and changes in the local geometric and electronic environment, can also strongly influence catalytic activity and selectivity.^{39, 46}

Defect engineering, such as the introduction of oxygen vacancies (V_O), has been shown to regulate catalyst selectivity and stability. Qiao *et al.*⁴⁷ reported that atomic Cu doping in SnO_2 induced the formation of V_O , which played a vital role in stabilizing the key $*\text{OCHO}$ intermediate and preserving the oxidation state of Sn, thereby improving catalyst stability. Hu *et al.*⁴⁸ further confirmed this effect using a V_O -enriched InOOH catalyst.

Inspired by the discussion above, this thesis investigates the synergistic effects of mesoporous structure and defect chemistry on the activity and stability of SnO_2 for CO_2RR . Additional to the structural and defect modifications, the influence of Sn doping in BiOCl on catalytic performance will be also comprehensively studied, extending the scope to the compositional tuning of Bi-based catalysts.

Chapter 3: Methodology

In this chapter, I introduce the experimental methods and the fundamental principles for characterization of both catalysts and catalytic reactions, and essential techniques used to track dynamic changes and reaction intermediates. The underlying physical principles necessary for interpreting the results are also discussed.

3.1 Materials synthesis and electrode preparation

In this thesis, the catalysts were synthesized using a soft-templating approach. As discussed in Section 2.2.2, this method offers several advantages, including improved structural control and tunable porosity, making it suitable for the preparation of the materials studied here. The electrodes were then prepared by a drop-casting method.

3.1.1 Materials synthesis

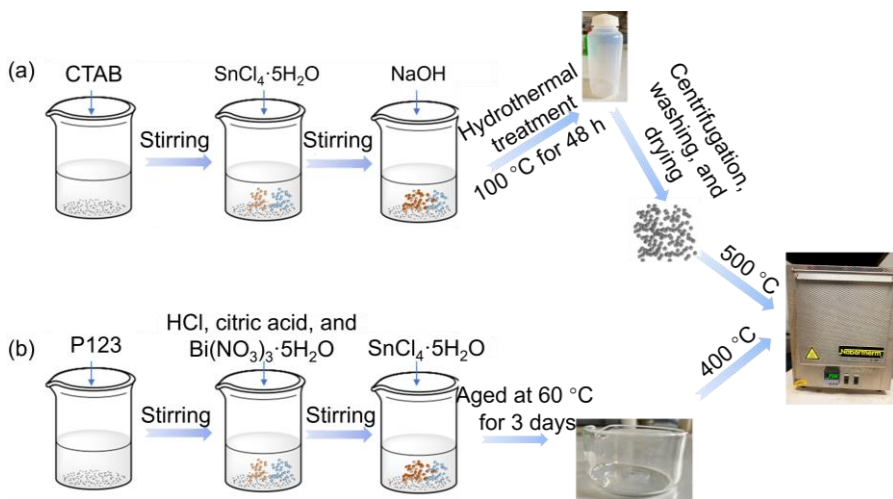


Figure 3.1 Schematic illustration of synthesis of mesoporous SnO₂ (a) and Sn-doped BiOCl samples (b).

Figure 3.1 shows the general synthesis protocols for mesoporous SnO₂ and Sn-doped BiOCl materials. In the first work, mesoporous

SnO₂ was prepared using a surfactant-assisted hydrothermal method. First, cetyltrimethylammonium bromide (CTAB) was dissolved in deionized water, followed by the addition of NaOH. An aqueous solution of SnCl₄·5H₂O was then added dropwise under stirring to form a homogeneous mixture. The color of the mixture turned white. Then the solution was transferred to a Teflon bottle and treated hydrothermally at 100 °C for 48 h. The obtained precipitate (white powder) was collected, washed, dried, and finally calcined at 500 °C to remove the template and crystallize the SnO₂ framework, yielding a light-yellow powder. More details can be found in Paper I.

In the second work, layered Sn-doped BiOCl samples were prepared by a sol–gel method. Pluronic P123 was first dissolved in ethanol, followed by the addition of HCl, citric acid, and Bi(NO₃)₃·5H₂O under stirring. A SnCl₄·5H₂O solution, prepared separately in HCl and water, was then added dropwise to the Bi precursor solution. After stirring to obtain a homogeneous sol, the mixture was aged at 60 °C for 3 days to form a gel. The obtained gel was subsequently calcined at 400 °C for 4 h to get the final product as a gray powder. More details can be found in Paper II.

3.1.2 Electrode preparation

For electrochemical measurements, electrodes were prepared using a drop-casting method (Figure 3.2). The catalyst ink was prepared by mixing 7 mg catalyst, 500 μL isopropanol, 450 μL deionized water, and 50 μL Nafion solution (as the binder). The suspension was sonicated for 2 h to obtain a homogeneous dispersion. Subsequently, 200 μL of the ink was drop-cast onto carbon paper and dried at room temperature.

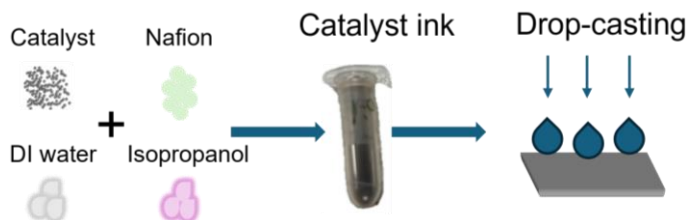


Figure 3.2 Schematic illustration of electrode preparation.

3.2 Electrochemical measurements

All electrochemical measurements in this thesis were carried out in an H-type cell separated by a Nafion 115 membrane (Figure 3.3). A standard three-electrode configuration was employed, consisting of a Pt plate as the counter electrode, an Ag/AgCl (saturated KCl) electrode as the reference electrode, and a catalyst-coated carbon paper as the working electrode.

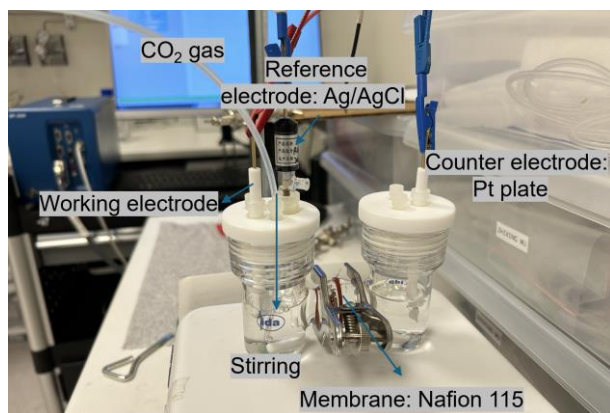


Figure 3.3 Setup for electrochemical measurements.

Various electrochemical techniques were applied to evaluate the catalytic properties from different perspectives. For consistency and ease of comparison, all potentials were initially measured versus the Ag/AgCl reference electrode and subsequently converted to the reversible hydrogen electrode (RHE) using the Nernst equation (Eq. 1). A potential drop (iR drop) arises from the internal resistance of the

electrolyte and the cell, causing the measured potential to deviate from the true electrode potential. However, no iR compensation was applied in this thesis to avoid possible overcorrection and to present the raw data.

$$E_{(vs. RHE)} = E_{(vs. Ag/AgCl)} + 0.059\text{pH} + 0.197 \quad (Eq. 1)$$

3.2.1 Voltammetry

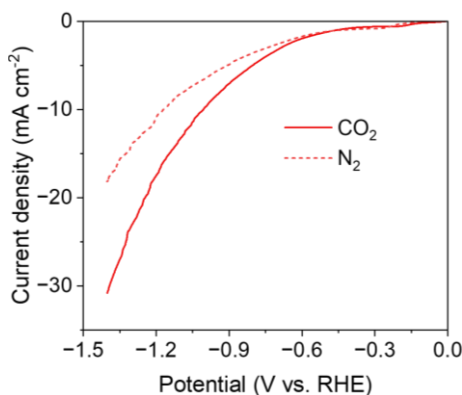


Figure 3.4 LSV curves recorded under CO_2 - and N_2 -saturated conditions.

Voltammetry is an electrochemical technique in which a time-dependent potential is applied to the working electrode and the resulting current is measured to probe redox processes at the electrode–electrolyte interface. The experiments are typically carried out in a three-electrode configuration (Figure 3.3). Linear sweep voltammetry (LSV) and cyclic voltammetry (CV) were the two primary techniques used in this thesis. LSV was conducted to compare the current densities measured in CO_2 - and N_2 -saturated 0.5 M KHCO_3 electrolytes. As shown in Figure 3.4, LSV curves were recorded in both CO_2 and N_2 atmospheres. Beyond -0.6 V vs. RHE, the current density measured in the CO_2 -saturated electrolyte is pronouncedly more negative than that obtained in the N_2 -saturated solution. This

difference suggests that the catalyst exhibits intrinsic catalytic activity toward the CO₂RR.

The electrochemically active surface area of the electrodes was estimated from the double-layer capacitance (C_{dl}). The C_{dl} values were determined by cyclic voltammetry (CV) performed at various scan rates within a non-Faradaic potential window in an H-type cell (Figure 3.5a). From the recorded CV curves, the difference between the anodic and cathodic current densities ($j_a - j_c$) at a selected potential was extracted. The capacitive current ($\Delta j/2$) was then plotted as a function of the scan rate (Figure 3.5(b)). According to Eq. 2, the slope of the linear fit corresponds to the double-layer capacitance of the electrode.⁴⁹

$$C_{dl} = \frac{1}{2} \times \frac{\partial(j_a - j_c)}{\partial(\text{scan rate})} \quad (\text{Eq. 2})$$

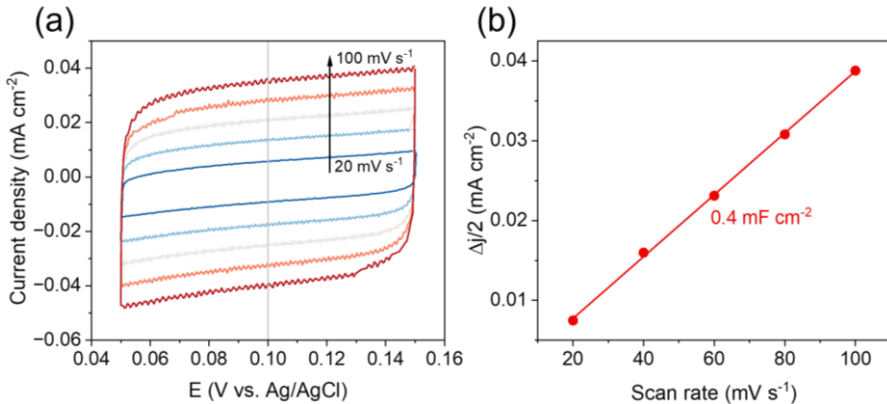


Figure 3.5 (a) CV curves recorded at different scan rates within the non-Faradaic potential window. (b) Plot of $\Delta j/2$ as a function of scan rate and the solid line is the linear fitting to the data.

3.2.2 Electrochemical impedance spectroscopy

Electrochemical impedance spectroscopy (EIS) is a powerful tool for analyzing reaction kinetics, the properties of the electric double layer, and mass transport processes. EIS is performed by applying a small

sinusoidal voltage perturbation at a fixed potential over a wide frequency range (typically from 100 kHz to 10 mHz). The resulting current response is analyzed in terms of its amplitude and phase shift, allowing the impedance of the system to be determined.

Electrical equivalent circuits can be used to model the obtained data to represent the working electrode interfacial region and processes. For example, the dashed line (a perfect semicircle) represents the response of an ideal RC circuit (Figure 3.6(a)). It can be described by a circuit including three components: R_s , the solution resistance; C_{dl} , the double layer capacitance; and R_{ct} , the charge transfer resistance. However, in most cases the complex-plane plot (Nyquist plot) does not provide a perfect semicircle and is often suppressed, as shown by the solid line in Figure 3.6(a). This behavior is attributed to surface non-uniformity, roughness, and even porosity, where each local submicroscopic region gives rise to its own RC combination. In such cases, C_{dl} is commonly replaced by a constant phase element (CPE) to describe the non-ideal capacitive behavior, which can be expressed by Eq. 3.⁵⁰

$$CPE = -\frac{1}{(i\omega C)^\alpha} \quad (Eq. 3)$$

where α is the CPE exponent, ranging from 1.0 for an ideal capacitor to 0.5 for an infinite Warburg impedance.⁵¹ ω is the radial frequency ($\omega = 2\pi f$).

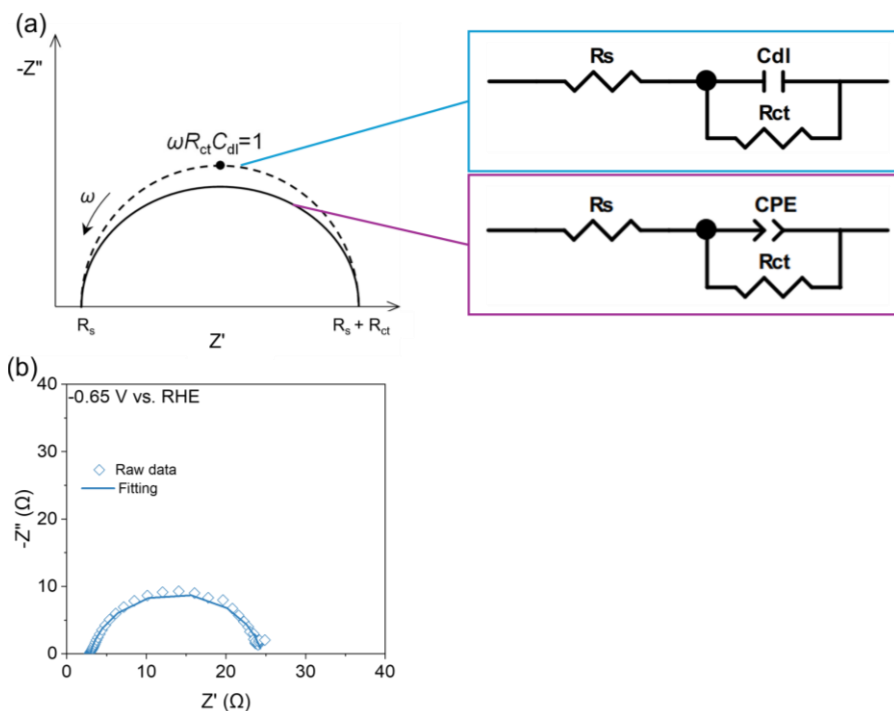


Figure 3.6 (a) Nyquist plots for selected equivalent circuits: an ideal capacitor (dashed line) and a non-ideal capacitor described by a constant phase element (CPE). Adapted from Ref. ⁵⁰. (b) Impedance plot and fitted by an R-CPE (non-ideal capacitor) equivalent circuit.

Figure 3.6(b) shows an example of a non-perfect semicircle obtained from the measurements and it can be associated with an R-CPE circuit. The impedance data can be fitted by ZView software to obtain the value of each circuit component. Generally, a small R_{ct} indicates a fast charge transfer process.

3.2.3 Chronoamperometry

Chronoamperometry (CA) is a potentiostatic method in which constant potential is applied to the working electrode, and the resulting current is recorded as a function of time. The catalysts were tested at different potentials, and the liquid products were collected for NMR

analysis. The potential that yielded to the highest Faradaic efficiency (FE, calculated according to Eq. 4) was selected for long-term stability tests. FE represents the fraction of the total charge consumed in an electrochemical process that contributes to the formation of a specific product (e.g., formate) and is widely used as a key metric for evaluating the selectivity of electrocatalysts.

$$FE_{(formate)} = \frac{n \times N \times F}{I \times t} \times 100\% \quad (Eq. 4)$$

where n is the number of moles of formate produced in the cathodic electrolyte, N is the number of electrons transferred to form the liquid product (e.g., 2 for formate), F is Faraday constant (96485 C mol^{-1}), t is the reaction time, and I is the average total current during electrolysis.

3.2.4 CO₂RR product analysis

¹H nuclear magnetic resonance (¹H NMR) is a technique that studies the magnetic properties of hydrogen nuclei in a magnetic field to determine the structure, environment, and interactions of hydrogen atoms in a molecule. It provides detailed information about molecular connectivity and chemical surroundings. The liquid products were analyzed by ¹H NMR using water suppression mode. Briefly, the collected electrolyte was mixed with deuterium oxide (D₂O) and dimethyl sulfoxide (DMSO) was added as the internal standard. The NMR spectrum was shown in Figure 3.7. The characteristic peak of formate (HCOO⁻) appears at approximately 8.4 ppm, while the signal of DMSO is observed at around 2.6 ppm.

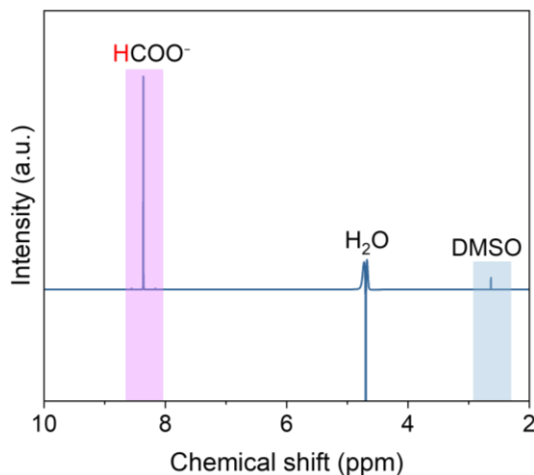


Figure 3.7 ^1H NMR spectrum of collected electrolyte after electrolysis.

3.3 Physical characterization

In this section, I will introduce various physical characterization methods applied in this thesis. A general overview of the characterization techniques is provided, covering the principles of instrumentation and data interpretation.

3.3.1 X-ray diffraction

X-ray diffraction (XRD) is widely used to identify the crystal structure, phases, and phase composition of crystalline materials. The principle of XRD is commonly described by Bragg diffraction (Figure 3.8), which follows Bragg's law (Eq. 5). This equation describes the relationship between the X-ray wavelength, the diffraction angle, and the lattice spacing.

$$n\lambda = 2d\sin(\theta) \quad (\text{Eq. 5})$$

where n is an integer representing the order of reflection, λ is the X-ray wavelength, d is the interplanar spacing, and θ is the diffraction angle.

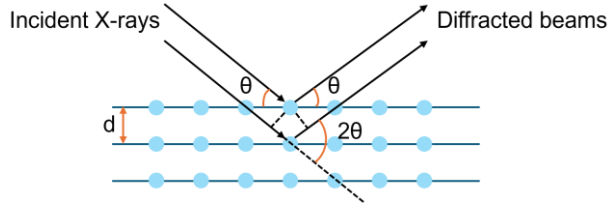


Figure 3.8 Schematic illustration of Bragg's law.

XRD results are typically presented as diffraction intensity as a function of the diffraction angle (2θ). Unit cell parameters can be determined from the 2θ peak positions, which are widely used for phase identification and assessing sample purity. Peak shape can also provide information about crystallinity, structural disorder, and defects, such as crystallite size and strain. In this thesis, the crystallite size (D) was estimated using the Scherrer equation (Eq. 6):

$$D = \frac{K\lambda}{\beta \cos\theta} \quad (\text{Eq. 6})$$

where K is the dimensionless shape factor and β is the full width at half maximum (FWHM) of the diffraction peaks in the XRD pattern.

3.3.2 Electron microscopy

Electron microscopy allows us to see the features of the materials in a high magnification even to atomic level, bringing us the direct view of the material from morphology to atomic crystal structure.

3.3.2.1 Scanning electron microscopy

Scanning electron microscopy (SEM) is widely used to investigate the morphology and surface structure of materials. In SEM, a focused electron beam generated by an electron gun is accelerated by an applied voltage (0.5 to 30 kV) and scanned across the surface of the sample. The interaction between electrons and matter produces various signals, including secondary electrons, backscattered electrons,

and characteristic X-rays (Figure 3.9(a)). These signals carry different types of information. In general, two types of electrons are commonly used for imaging: backscattered electrons and secondary electrons. backscattered electrons originate from deeper regions of the sample, whereas secondary electrons are emitted mainly from the surface. backscattered electron images provide atomic number contrast, where regions with higher atomic numbers appear brighter. In contrast, secondary electron imaging reveals more detailed surface morphology.

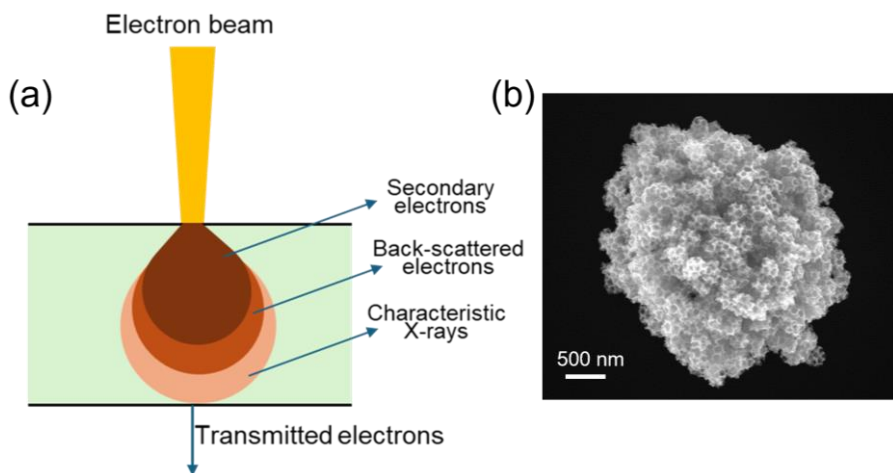


Figure 3.9 (a) Electron—matter interactions: different types of signals are generated. (b) SEM image of SnO₂ nanoflower.

In this thesis, SEM was mainly used to observe the overall morphology of the synthesized catalysts. For instance, the SnO₂ material shown in Figure 3.9(b) was imaged using an InLens detector at an accelerating voltage of 10 kV.

3.3.2.2 Transmission electron microscopy

Transmission electron microscopy (TEM) forms images by transmitting a high-energy electron beam through a thin specimen.⁵² TEM is typically operated at an accelerating voltage of 30-300 kV,

which allows much higher magnification and spatial resolution than SEM. For TEM imaging, the specimen should be sufficiently thin (~ 100 nm) to allow electrons to pass through the material and it needs to be operated under high-vacuum conditions to maximize the mean free path of electrons.

Scanning transmission electron microscopy (STEM) integrates imaging concepts from both TEM and SEM. In STEM, a finely focused electron beam is scanned across the sample in a raster pattern. Different imaging modes arise from variations in the detector collection angle. Among these modes, high-angle annular dark-field (HAADF) imaging is widely used, as illustrated in Figure 3.10(a). A key component of HAADF-STEM is an annular detector, which selectively collects electrons scattered to high angles. The intensity of high-angle scattering is approximately proportional to the square of the atomic number (Z^2), a phenomenon commonly referred to as Z-contrast. As a result, in HAADF images, elements with higher atomic numbers appear brighter, while elements with lower atomic numbers appear darker. This contrast mechanism enables intuitive differentiation and localization of elements within a sample. For example, HAADF-STEM imaging was performed on the BiOCl sample used in this thesis, confirming its layered structure (Figure 3.10(b)).

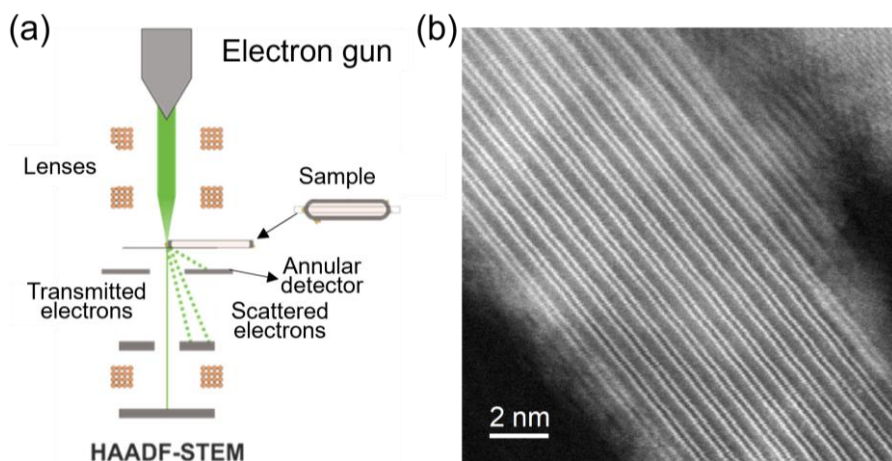


Figure 3.10 (a) Schematic illustration of HAADF-STEM. Adopted from Ref. ⁵³. (b) HAADF-STEM image of layered BiOCl used in this thesis.

3.3.3 X-ray photoelectron spectroscopy

X-ray photoelectron spectroscopy (XPS) is used to analyze the surface chemical composition and electronic states of materials under ultra-high vacuum conditions.⁵⁴ As illustrated in Figure 3.11, the sample is irradiated with X-rays of known photon energy, which induces the photoelectric effect and results in the emission of photoelectrons from atoms near the surface. The kinetic energy of the emitted electrons is measured by an electron energy analyzer, and the electron binding energy (E_B) can be calculated according to Eq. 7.

$$E_B = E_P - E_K \quad (\text{Eq. 7})$$

where E_P is the energy of the incident photon (e.g., a monochromatic Al $K\alpha$ X-ray source with energy of 1486.6 eV, operating at 15 kV and 25 W) and E_K is the kinetic energy of the emitted electron.

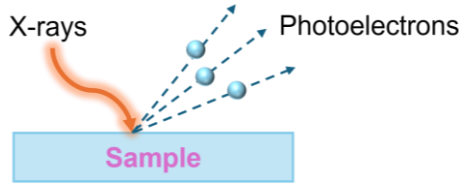


Figure 3.11 Schematic of XPS process.

3.3.4 Physisorption

Physisorption is a technique used to determine the specific surface area (SSA), pore volume, and pore size distribution of porous materials. The results are typically represented by adsorption isotherms, which plot the amount of gas adsorbed on the solid surface as a function of the relative pressure. According to the International Union of Pure and Applied Chemistry (IUPAC), adsorption isotherms can be divided into six types, with four types of hysteresis loops (Figure 3.12).⁵⁵

To analyze these isotherms, the most commonly used method for estimating SSA is the Brunauer–Emmett–Teller (BET) method,⁵⁶ which can be expressed by Eq. 8.

$$\frac{P}{V(P_0 - P)} = \frac{1}{V_m C} + \frac{C - 1}{V_m C} \times \frac{P}{P_0} \quad (\text{Eq. 8})$$

Where V is the adsorbed gas volume, P is the equilibrium pressure, P_0 is the saturation vapor pressure of the adsorbate at the measurement temperature, V_m is the monolayer adsorption capacity, and C is the BET constant related to the adsorption energy. This equation is typically applied over the relative pressure range of $0.05 < P/P_0 < 0.30$.

Then the SSA determined by BET can be calculated using Eq. 9.⁵⁷

$$SSA = \frac{A_S}{m} = \frac{n_m N_A \sigma}{m} \quad (\text{Eq. 9})$$

where A_s is the total surface area, m is the mass of the sample, N_A is the Avogadro constant, and σ is the cross-sectional area of the adsorbate molecule.

According to IUPAC classifications, mesoporous materials mainly produce type IV isotherms. At low relative pressures, gas molecules first form a single layer on the pore walls and then build up additional layers. As the pressure rises further, the gas condenses inside the mesopores, a process known as capillary condensation, and the adsorbed amount increases sharply. Once all the pores are filled, the curve flattens into a plateau. During desorption the gas does not escape the same pressures at which it entered, so the adsorption and desorption curves trace out different paths and form a hysteresis loop. Point B, which appears in both type II and type IV isotherms, marks the stage at which the first complete monolayer has formed, and multilayer adsorption begins (Figure 3.12(a)).

The shape of the hysteresis loop varies with pore geometry, and four main types are distinguished (Figure 3.12(b)). H_1 loops have two steep, nearly parallel branches and are seen in materials with regular, cylindrical pores that are open at both ends. H_2 loops rise slowly on adsorption but drop steeply on desorption, which is typical of ink-bottle-shaped pores or tangled pore networks where the narrow openings delay gas escape. H_3 loops do not level off at high pressures and occur when flat, plate-like particles stack together to create slit-shaped gaps. H_4 loops look similar to H_3 but stay relatively flat over a broader pressure range and close earlier, suggesting narrow slits in solids that contain both very small micropores and larger mesopores.

In this thesis, N_2 physisorption was used to determine the specific surface area and pore size distribution of the mesoporous SnO_2 studied in Paper I. Meanwhile, the results indicate that mesoporous SnO_2 exhibited type IV isotherms with an H_2 hysteresis loop.

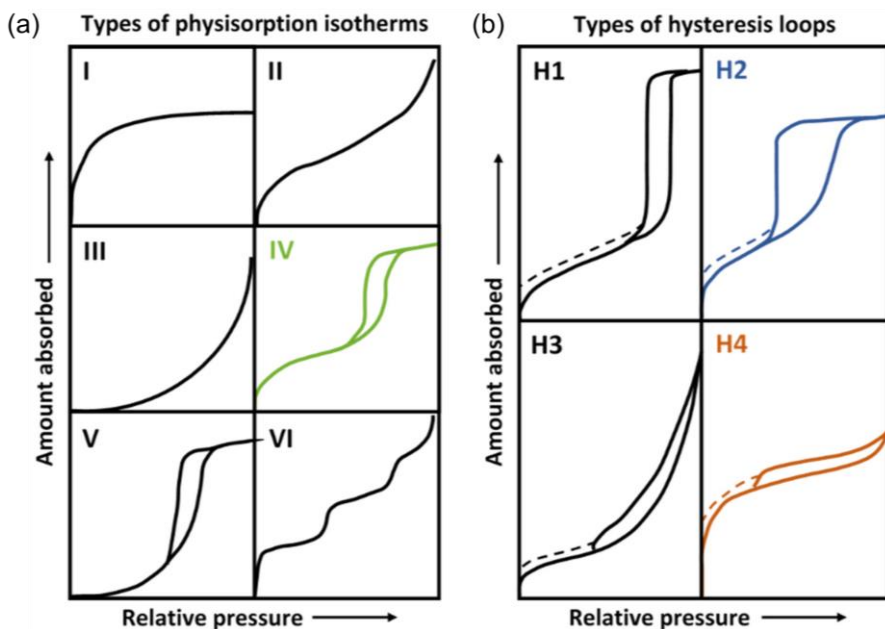


Figure 3.12 (a) The six types of physisorption isotherms. (b) The four types of hysteresis loops. Both are classified according to the IUPAC.⁵⁵ Reproduced from Ref. ⁵⁸.

3.4 In situ characterization of CO₂RR

In this section, I will introduce various in situ characterization methods that are crucial for understanding the reaction mechanism and catalysts evolution under reaction conditions. These techniques play a key role in the rational design of catalysts.

3.4.1 Vibrational spectroscopy

Vibrational spectroscopy can provide vast information regarding both the reactants and catalysts' surface, which are the two important components of the electrocatalytic reaction. Light is divided into different ranges depending on the photon frequency. Ultraviolet and visible light is used in Raman spectroscopy, while infrared light is used in IR spectroscopy.⁵⁹ In this thesis, Raman and IR spectroscopy are

used to understand the dynamic changes of catalysts and the evolution of reaction intermediates.

3.4.1.1 Raman spectroscopy

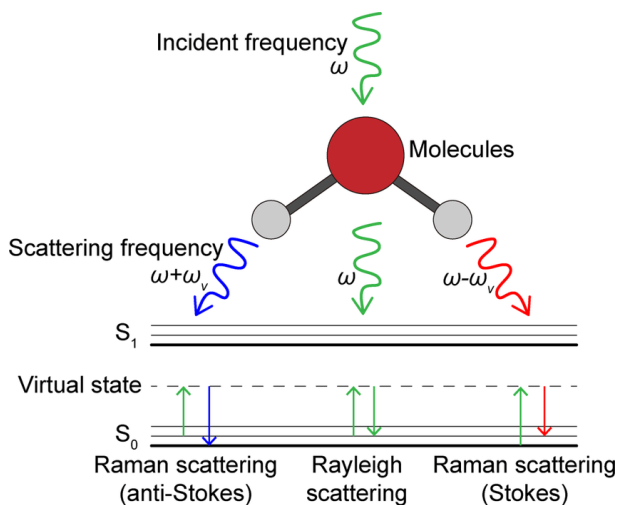


Figure 3.13 Scheme and Jablonski diagram of Raman scattering and Rayleigh scattering. Reproduced from Ref. ⁶⁰.

Raman spectroscopy arises from the inelastic scattering of light when incident photons interact with molecules and differentiate from elastic (Rayleigh) scattering (Figure 3.13). In Raman scattering, the scattered photons exhibit a frequency shift relative to the incident light (ω). When an incident photon interacts with a molecule in its vibrational ground state, part of the photon energy is transferred to the molecule, promoting it to an excited vibrational level. The scattered photon emerges with a lower frequency ($\omega - \omega_v$), this process is referred to as the Stokes shift. Conversely, if the molecule already resides in an excited vibrational state before the collision, it can relax to the ground state during scattering and transfer its vibrational energy to the photon, which is then emitted at a higher frequency ($\omega + \omega_v$), this is known as the anti-Stokes shift. In most cases, the Stokes signal is much stronger than the anti-Stokes signal because most molecules at room

temperature occupy the vibrational ground state according to the Boltzmann distribution.⁶⁰ Consequently, Raman spectroscopy typically measures Stokes signals.

An in situ Raman measurement typically includes an in situ cell, a peristaltic pump, a potentiostat, and a Raman spectrometer. As shown in Figure 3.14, the cell employs a three-electrode configuration consisting of a counter electrode (CE, Pt wire), a reference electrode (RE, Ag/AgCl), and a working electrode (WE, the catalyst). These electrodes are connected to a potentiostat to apply an electrochemical bias, either at a constant potential (chronoamperometry) or under a constant current (chronopotentiometry) depending on the purpose of the measurement. A peristaltic pump is used to circulate the CO₂-saturated 0.5 M KHCO₃ electrolyte. During the measurement, the laser is focused on the catalyst surface, and the Raman signals are collected by the spectrometer. In this thesis, in situ Raman spectroscopy was used to investigate the dynamic structural changes of the catalysts during the CO₂RR process.

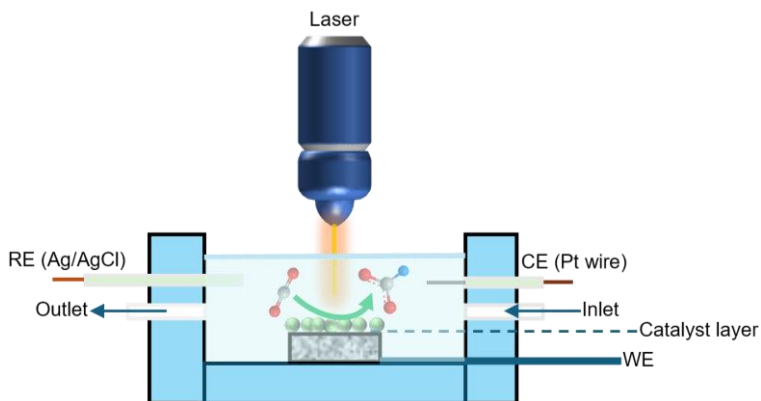


Figure 3.14 Schematic illustration of in situ Raman measurements.

3.4.1.2 Infrared spectroscopy

IR spectroscopy measures the absorption and emission of infrared radiation by molecules. It provides fingerprint information about molecular structures and chemical compositions. The IR signal arises from the interaction between infrared radiation and molecular vibrations associated with chemical bonds in a sample. IR spectroscopy can be used to analyze various types of samples, including solids, liquids, gases, and polymers. The resulting IR spectrum is typically presented as absorbance or transmittance as a function of the frequency or wavenumber of the infrared radiation.

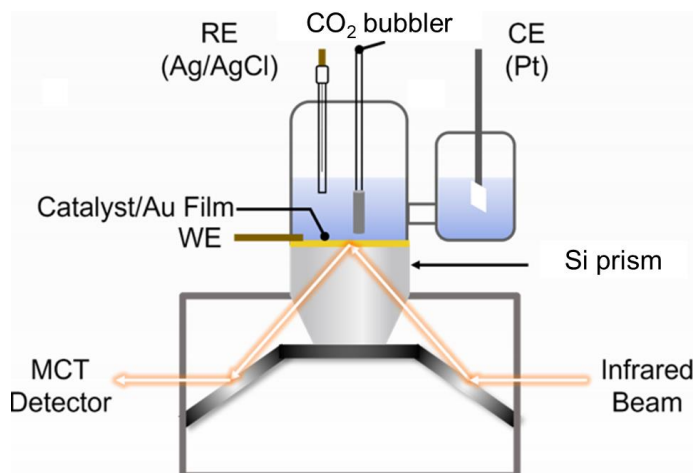


Figure 3.15 Illustration of in situ ATR-SEIRAS measurements.

Based on IR spectroscopy and combined with electrochemical techniques, attenuated total reflection surface-enhanced infrared absorption spectroscopy (ATR-SEIRAS) has emerged as a powerful and highly surface-sensitive tool for analyzing molecules present at electrode surfaces (Figure 3.15). To perform in situ ATR-SEIRAS measurements, an ATR accessory is used to direct the infrared beam, together with an ATR crystal coated with a thin Au film, on which the catalysts are deposited. In addition, a spectroelectrochemical cell with a three-electrode configuration and a CO₂ bubbler is employed, along

with a potentiostat to control the electrochemical reaction, following a procedure like that used for the in situ Raman measurements discussed above. During the CO₂RR process, the IR signals are recorded using a MCT detector, which offers high sensitivity and a fast response time suitable for capturing the weak and transient spectral features of reaction intermediates under in situ conditions.

3.4.2 X-ray based techniques

X-ray techniques are complementary to vibrational spectroscopy and help overcome the limitations in probing catalyst structure and composition. In this section, two typical and widely used X-ray-based techniques are presented.

3.4.2.1 X-ray absorption spectroscopy

X-ray absorption spectroscopy (XAS) has become one of the most important techniques for providing valuable information about the dynamic changes in catalysts under reaction conditions. It is applicable to a wide range of materials, including ordered, disordered, nanostructured, and liquid systems.

An XAS spectrum can be divided into two regions: X-ray absorption near-edge structure (XANES) and extended X-ray absorption fine structure (EXAFS), which provide information about the electronic structure and the coordination environment (Figure 3.16).⁶¹ The XANES region typically spans approximately 50–200 eV above the absorption edge and reflects electronic transitions from core levels to unoccupied states, providing information about the oxidation state of the catalyst.⁶² The EXAFS signal originates from interference effects caused by the backscattering of photoelectrons from neighboring atoms. It appears as an oscillatory component in the absorption spectrum above the absorption edge and is mainly dominated by single-scattering events. Analysis of EXAFS can reveal

the local coordination environment around the absorbing atom, including the type of neighboring atoms, coordination number, and interatomic distances.^{63, 64}

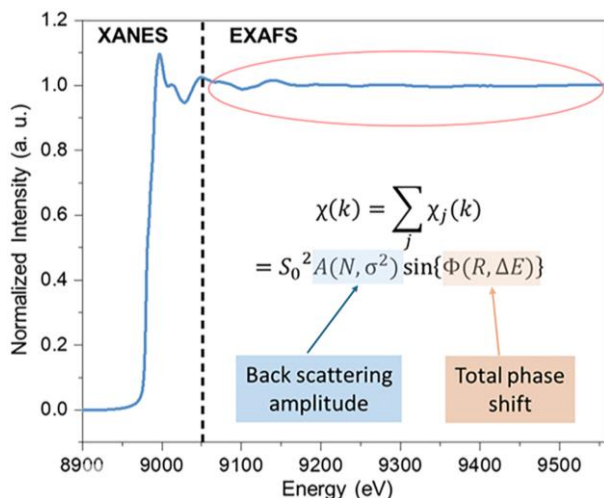


Figure 3.16 A typical XAS spectrum consisting of XANES and EXAFS regions, with the inset showing the quantitative analysis of EXAFS spectra. Reproduced from Ref. ⁶⁴.

To perform in situ XAS measurements at a beamline, one of the key factors is the design of an in situ cell that is compatible with the experimental configuration of the beamline. Here, I designed and customized an in situ cell (Figure 3.17) suitable for our measurements, which can operate in both fluorescence and transmission modes.

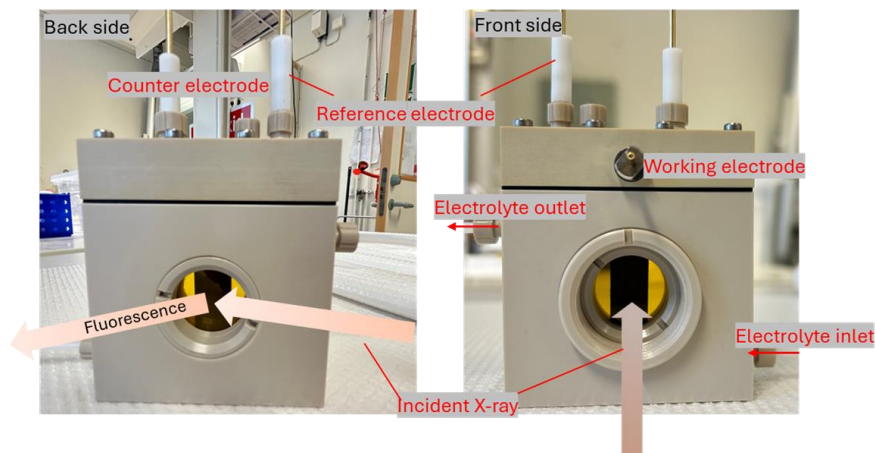


Figure 3.17 Schematic illustration of a customized in situ XAS cell.

3.4.2.2 X-ray diffraction

The principle of XRD has been discussed in Section 3.3.3. Here, I mainly discuss the application of XRD in in situ measurements. Depending on the X-ray source, in situ XRD measurements can generally be divided into two types: those based on conventional laboratory X-ray sources and those performed at synchrotron radiation facilities. Compared with laboratory instruments, synchrotron XRD is carried out under substantially higher photon flux, with superior angular resolution and excellent time resolution (at the millisecond level), enabling the detection of rapid structural changes during CO₂RR. Analysis of in situ XRD patterns yields information on the crystal structure, phase transformations, and crystallite size of the working catalysts. At certain synchrotron beamlines, XRD and XAS data can be collected simultaneously, so that changes in valence state and local coordination environment are captured together with the long-range structural evolution. This combination of techniques is particularly valuable for linking catalytic performance to structural features and for guiding catalyst design.

Chapter 4: Summary of included papers

In this thesis, two main catalyst systems were explored. The first study investigates how mesopores and oxygen vacancies in SnO₂ jointly enhance CO₂ electroreduction, while the second focuses on the influence of Sn doping on the structural evolution of Bi-based electrocatalysts. The two studies provide mechanistic insights that can guide the rational design of efficient and stable catalysts for CO₂RR.

4.1 Paper I

To elucidate the effect of mesostructure and defect chemistry on catalytic performance, mesoporous SnO₂ was synthesized as a model catalyst and compared with nonporous counterparts. The mesoporous SnO₂ exhibited enhanced formate selectivity, showing a 45.4% relative increase compared with bulk SnO₂, together with improved stability, as indicated by a lower Faradaic efficiency loss after 12 h of electrolysis. Electrochemical analysis, in situ spectroscopic characterization, and density functional theory calculations revealed that the mesoporous structure facilitates CO₂ adsorption and interfacial charge transfer, while oxygen vacancies stabilize key *OCHO intermediates and lower the reaction energy barrier. Moreover, the mesostructure promoted the formation of oxygen vacancies, which helped maintain the oxidation state of Sn under reaction conditions and contributed to improved catalyst durability. These findings demonstrate the synergistic roles of mesoporosity and oxygen vacancies in regulating CO₂RR activity and stability, providing insights into the design of efficient Sn-based electrocatalysts for CO₂RR.

4.2 Paper II

The role of Sn doping in regulating the structural evolution and catalytic performance of layered BiOCl during CO₂RR was investigated. Sn-doped BiOCl nanoplates were synthesized via a sol-gel method and used as electrocatalysts for CO₂ conversion to formate. Structural characterization combining in situ Raman spectroscopy, time-resolved ex situ XRD, and S/TEM analyses revealed that both pristine and Sn-doped BiOCl undergo electrochemical reconstruction under reaction conditions, yielding metallic Bi with preferentially exposed crystal facets. While the reconstructed catalysts predominantly expose the Bi 012 facet, Sn doping also promotes additional exposure of the Bi 003 facet, suggesting that the dopant influences both the reconstruction pathway and the arrangement of active sites. Electrochemical measurements indicated that a doping level of approximately 5% Sn achieves the highest formate selectivity, with a Faradaic efficiency of ~87.7% at -1.0 V vs. RHE, considerably higher than that of undoped BiOCl. In situ ATR-SEIRAS further showed that Sn facilitates *OCHO adsorption and enhances water dissociation, both of which are crucial for formate formation. These observations emphasize the role of dopant-regulated surface reconstruction and facet exposure in determining catalytic activity and provide guidance for designing efficient Bi-based electrocatalysts for CO₂RR.

Chapter 5: Outlook

For Paper I, although mesoporous SnO₂ was obtained, the pores are mainly interparticle pores. Further efforts can therefore be devoted to tuning the pore structure, which can provide additional opportunities for improving CO₂RR performance. Materials with intraparticle pore structures may provide more accessible active sites for the reaction. To achieve this, a range of templates and synthesis conditions, such as pH and temperature, can be explored.

In addition to the results presented in Paper II, I also intend to combine the in situ XAS and XRD data to further elucidate the dynamic structural evolution of the catalysts in terms of valence states, composition, and phase evolution. This combined analysis can provide multiscale information about the reaction mechanism. Meanwhile, more efforts will be dedicated to uncovering the general principles that govern catalysts reconstruction and reaction pathways, such as the roles of dopants, effects, and the electrolyte environment, which are essential for guiding the rational design of efficient and stable CO₂RR electrocatalysts.

This thesis mainly employs the conventional H-cell and focuses on fundamental studies of the structure–performance relationships of catalysts. Nevertheless, the limitations of the H-cell are also recognized, including relatively low current densities and limited CO₂ mass transport. Based on this, it is also important to evaluate catalytic performance under more practical configurations, for example using a flow cell with a GDE or an MEA cell, as discussed in Section 2.1.1. After initial evaluation at the laboratory scale (1 cm²), electrodes showing promising performance could be further assessed at a larger scale (100 cm²) in collaboration with industrial partners.

Inspired by the findings in Paper I and II, I found that catalyst reconstruction plays a key role in determining catalyst stability. For further optimization of the catalyst, controlling excessive or deep reconstruction is essential for improving catalyst durability. This is also crucial for enabling reliable scale-up to larger reactor systems.

References

- (1) *Greenhouse gases*. World Meteorological Organization, <https://wmo.int/topics/greenhouse-gases>.
- (2) Susan Tierney, L. B. *Setting the Record Straight About Renewable Energy*. World Resources Institute, <https://www.wri.org/insights/setting-record-straight-about-renewable-energy>.
- (3) Kähler, F.; Carus, M.; Porc, O.; vom Berg, C. Turning off the Tap for Fossil Carbon: Future Prospects for a Global Chemical and Derived Material Sector Based on Renewable Carbon. *Industrial Biotechnology* **2021**, *17* (5), 245-258. DOI: 10.1089/ind.2021.29261.fka.
- (4) *The Future of Petrochemicals*. IEA (2018), <https://www.iea.org/reports/the-future-of-petrochemicals>.
- (5) Vos, R. E.; Sun, P.; Schauer mann, D.; Javed, H.; Hanselman, S. R.; Fu, G.; Koper, M. T. M. CO₂ electroreduction on Cu operates via an alternative chain growth mechanism to form C–C bonds at elevated temperature and pressure. *Nature Catalysis* **2025**, *8* (12), 1338-1347. DOI: 10.1038/s41929-025-01451-1.
- (6) Kaneco, S.; Iiba, K.; Ohta, K.; Mizuno, T.; Saji, A. Electrochemical reduction of CO₂ on Au in KOH + methanol at low temperature. *Journal of Electroanalytical Chemistry* **1998**, *441* (1), 215-220. DOI: [https://doi.org/10.1016/S0022-0728\(97\)00438-5](https://doi.org/10.1016/S0022-0728(97)00438-5).
- (7) Jiang, Y.; Huang, L.; Chen, C.; Zheng, Y.; Qiao, S.-Z. Catalyst–electrolyte interface engineering propels progress in acidic CO₂ electroreduction. *Energy & Environmental Science* **2025**, *18* (5), 2025-2049, 10.1039/D4EE05715E. DOI: 10.1039/D4EE05715E.
- (8) Luo, W.; Zhang, J.; Li, M.; Züttel, A. Boosting CO Production in Electrocatalytic CO₂ Reduction on Highly Porous Zn Catalysts. *ACS Catalysis* **2019**, *9* (5), 3783-3791. DOI: 10.1021/acscatal.8b05109.
- (9) Yao, Z.; He, X.; Lin, R. Electrochemical Carbon Dioxide Reduction in Acidic Media. *Electrochemical Energy Reviews* **2024**, *7* (1), 8. DOI: 10.1007/s41918-024-00210-3.
- (10) Weekes, D. M.; Salvatore, D. A.; Reyes, A.; Huang, A.; Berlinguette, C. P. Electrolytic CO₂ Reduction in a Flow Cell. *Accounts of Chemical Research* **2018**, *51* (4), 910-918. DOI: 10.1021/acs.accounts.8b00010.

- (11) Xu, D.; Li, K.; Jia, B.; Sun, W.; Zhang, W.; Liu, X.; Ma, T. Electrocatalytic CO₂ reduction towards industrial applications. *Carbon Energy* **2023**, *5* (1), e230. DOI: <https://doi.org/10.1002/cey2.230>.
- (12) Lai, W.; Qiao, Y.; Zhang, J.; Lin, Z.; Huang, H. Design strategies for markedly enhancing energy efficiency in the electrocatalytic CO₂ reduction reaction. *Energy & Environmental Science* **2022**, *15* (9), 3603-3629, 10.1039/D2EE00472K. DOI: 10.1039/D2EE00472K.
- (13) Lee, C. W.; Kim, C.; Min, B. K. Theoretical insights into selective electrochemical conversion of carbon dioxide. *Nano Convergence* **2019**, *6* (1), 8. DOI: 10.1186/s40580-019-0177-2.
- (14) Feaster, J. T.; Shi, C.; Cave, E. R.; Hatsukade, T.; Abram, D. N.; Kuhl, K. P.; Hahn, C.; Nørskov, J. K.; Jaramillo, T. F. Understanding Selectivity for the Electrochemical Reduction of Carbon Dioxide to Formic Acid and Carbon Monoxide on Metal Electrodes. *ACS Catalysis* **2017**, *7* (7), 4822-4827. DOI: 10.1021/acscatal.7b00687.
- (15) Wang, X.; Wang, Z.; García de Arquer, F. P.; Dinh, C.-T.; Ozden, A.; Li, Y. C.; Nam, D.-H.; Li, J.; Liu, Y.-S.; Wicks, J.; et al. Efficient electrically powered CO₂-to-ethanol via suppression of deoxygenation. *Nature Energy* **2020**, *5* (6), 478-486. DOI: 10.1038/s41560-020-0607-8.
- (16) Birdja, Y. Y.; Pérez-Gallent, E.; Figueiredo, M. C.; Göttle, A. J.; Calle-Vallejo, F.; Koper, M. T. M. Advances and challenges in understanding the electrocatalytic conversion of carbon dioxide to fuels. *Nature Energy* **2019**, *4* (9), 732-745. DOI: 10.1038/s41560-019-0450-y.
- (17) Arán-Ais, R. M.; Gao, D.; Roldan Cuenya, B. Structure- and Electrolyte-Sensitivity in CO₂ Electroreduction. *Accounts of Chemical Research* **2018**, *51* (11), 2906-2917. DOI: 10.1021/acs.accounts.8b00360.
- (18) Lee, H.; Park, N.; Kong, T.-H.; Kwon, S.; Shin, S.; Cha, S. G.; Lee, E.; Cha, J.; Sultan, S.; Kwon, Y. Advancements in electrochemical methanol synthesis from CO₂: Mechanisms and catalyst developments. *Nano Energy* **2024**, *130*, 110099. DOI: <https://doi.org/10.1016/j.nanoen.2024.110099>.
- (19) Wang, G.; Chen, J.; Ding, Y.; Cai, P.; Yi, L.; Li, Y.; Tu, C.; Hou, Y.; Wen, Z.; Dai, L. Electrocatalysis for CO₂ conversion: from fundamentals to value-added products. *Chemical Society Reviews*

- 2021**, *50* (8), 4993-5061, 10.1039/D0CS00071J. DOI: 10.1039/D0CS00071J.
- (20) DuanMu, J.-W.; Yang, X.-P.; Gao, F.-Y.; Atapour, M.; Gao, M.-R. Progress of mechanistic pathways involved in electrochemical CO₂ reduction. *Journal of Energy Chemistry* **2025**, *102*, 745-767. DOI: <https://doi.org/10.1016/j.jechem.2024.11.032>.
- (21) Qiao, J.; Liu, Y.; Hong, F.; Zhang, J. A review of catalysts for the electroreduction of carbon dioxide to produce low-carbon fuels. *Chemical Society Reviews* **2014**, *43* (2), 631-675, 10.1039/C3CS60323G. DOI: 10.1039/C3CS60323G.
- (22) Lu, Q.; Jiao, F. Electrochemical CO₂ reduction: Electrocatalyst, reaction mechanism, and process engineering. *Nano Energy* **2016**, *29*, 439-456. DOI: <https://doi.org/10.1016/j.nanoen.2016.04.009>.
- (23) Li, P.; Yang, F.; Li, J.; Zhu, Q.; Xu, J. W.; Loh, X. J.; Huang, K.-W.; Hu, W.; Lu, J. Nanoscale Engineering of P-Block Metal-Based Catalysts Toward Industrial-Scale Electrochemical Reduction of CO₂. *Advanced Energy Materials* **2023**, *13* (34), 2301597. DOI: <https://doi.org/10.1002/aenm.202301597>.
- (24) Han, N.; Ding, P.; He, L.; Li, Y.; Li, Y. Promises of Main Group Metal-Based Nanostructured Materials for Electrochemical CO₂ Reduction to Formate. *Advanced Energy Materials* **2020**, *10* (11), 1902338. DOI: <https://doi.org/10.1002/aenm.201902338>.
- (25) Zou, J.; Liang, G.; Lee, C.-Y.; Wallace, G. G. Progress and perspectives for electrochemical CO₂ reduction to formate. *Materials Today Energy* **2023**, *38*, 101433. DOI: <https://doi.org/10.1016/j.mtener.2023.101433>.
- (26) Back, S.; Kim, J.-H.; Kim, Y.-T.; Jung, Y. On the mechanism of high product selectivity for HCOOH using Pb in CO₂ electroreduction. *Physical Chemistry Chemical Physics* **2016**, *18* (14), 9652-9657, 10.1039/C6CP00542J. DOI: 10.1039/C6CP00542J.
- (27) Yang, Z.; Oropeza, F. E.; Zhang, K. H. L. P-block metal-based (Sn, In, Bi, Pb) electrocatalysts for selective reduction of CO₂ to formate. *APL Materials* **2020**, *8* (6). DOI: 10.1063/5.0004194 (accessed 3/1/2026).
- (28) Deng, W.; Zhang, L.; Li, L.; Chen, S.; Hu, C.; Zhao, Z.-J.; Wang, T.; Gong, J. Crucial Role of Surface Hydroxyls on the Activity and Stability in Electrochemical CO₂ Reduction. *Journal of the American Chemical Society* **2019**, *141* (7), 2911-2915. DOI: 10.1021/jacs.8b13786.

- (29) Luc, W.; Collins, C.; Wang, S.; Xin, H.; He, K.; Kang, Y.; Jiao, F. Ag–Sn Bimetallic Catalyst with a Core–Shell Structure for CO₂ Reduction. *Journal of the American Chemical Society* **2017**, *139* (5), 1885-1893. DOI: 10.1021/jacs.6b10435.
- (30) Liu, F.; Wang, J.; Ren, X.; Wu, H.; Zhao, J.; Zhang, J.; Xie, W.; Wang, G.; Han, X.; Deng, Y.; et al. In-situ reconstructed In doped SnO₂ amorphous–crystalline heterostructure for highly efficient CO₂ electroreduction with a dynamic structure-function relationship. *Applied Catalysis B: Environment and Energy* **2024**, *352*, 124004. DOI: <https://doi.org/10.1016/j.apcatb.2024.124004>.
- (31) Xie, X.; Li, G.; Geng, S. Y doping induced stability of Bi₂O₃ for efficient electrocatalytic reduction of CO₂ to formate. *Journal of Environmental Chemical Engineering* **2025**, *13* (5), 117570. DOI: <https://doi.org/10.1016/j.jece.2025.117570>.
- (32) Tian, B.; Wu, H.; Zhang, Y.; Chen, C.; Abdalla, K. K.; Sendeku, M. G.; Zhou, L.; Yu, J.; Wang, Y.; Kuang, Y.; et al. Cu-Induced Interfacial Water Engineering of SnO₂ for Durable and Highly Selective CO₂ Electroreduction. *ACS Catalysis* **2024**, *14* (14), 10904-10912. DOI: 10.1021/acscatal.4c01670.
- (33) Wang, Y.; Li, G.; Feng, J.; Wang, X.; Xue, Q.; Cheng, A.; Liu, B.; Zeng, S.; Wang, M.; Zhang, X. Boosting Electrochemical CO₂ Reduction to Formate over La-Doped SnO₂ via Pinning Effect and Water Activation. *Journal of the American Chemical Society* **2025**, *147* (44), 40126-40135. DOI: 10.1021/jacs.5c03978.
- (34) Sui, P.-F.; Gao, M.-R.; Wang, Y.-C.; Liu, S.; Luo, J.-L. Leveraging Inherent Structure of Tin Oxide for Efficient Carbonaceous Products Electrosynthesis. *Advanced Energy Materials* **2024**, *14* (33), 2401202. DOI: <https://doi.org/10.1002/aenm.202401202>.
- (35) Yang, S.; An, H.; Arnouts, S.; Wang, H.; Yu, X.; de Ruiter, J.; Bals, S.; Altantzis, T.; Weckhuysen, B. M.; van der Stam, W. Halide-guided active site exposure in bismuth electrocatalysts for selective CO₂ conversion into formic acid. *Nature Catalysis* **2023**, *6* (9), 796-806. DOI: 10.1038/s41929-023-01008-0.
- (36) Liu, G.; Li, Z.; Shi, J.; Sun, K.; Ji, Y.; Wang, Z.; Qiu, Y.; Liu, Y.; Wang, Z.; Hu, P. Black reduced porous SnO₂ nanosheets for CO₂ electroreduction with high formate selectivity and low overpotential. *Applied Catalysis B: Environmental* **2020**, *260*, 118134. DOI: <https://doi.org/10.1016/j.apcatb.2019.118134>.

- (37) Ma, Y.; Xiao, T.; Zhu, K.; Zhang, W.; Yin, Z.; Dong, A.; Sun, Z.; Zhao, D.; Li, W. Industry-Level Electrocatalytic CO₂ to CO Enabled by 2D Mesoporous Ni Single Atom Catalysts. *Angewandte Chemie International Edition* **2025**, *64* (5), e202416629. DOI: <https://doi.org/10.1002/anie.202416629>.
- (38) Li, Z.; Sun, B.; Xiao, D.; Liu, H.; Wang, Z.; Liu, Y.; Zheng, Z.; Wang, P.; Dai, Y.; Huang, B.; et al. Mesostructure-Specific Configuration of *CO Adsorption for Selective CO₂ Electroreduction to C₂₊ Products. *Angewandte Chemie International Edition* **2025**, *64* (1), e202413832. DOI: <https://doi.org/10.1002/anie.202413832>.
- (39) Amer, M. S.; AlOrajib, H. A.; Huang, K.-W.; Al-Mayouf, A. M. Gray mesoporous SnO₂ catalyst for CO₂ electroreduction with high partial current density and formate selectivity. *Environmental Research* **2024**, *252*, 118897. DOI: <https://doi.org/10.1016/j.envres.2024.118897>.
- (40) Yang, P.; Zhao, D.; Margolese, D. I.; Chmelka, B. F.; Stucky, G. D. Generalized syntheses of large-pore mesoporous metal oxides with semicrystalline frameworks. *Nature* **1998**, *396* (6707), 152-155. DOI: 10.1038/24132.
- (41) Feng, D.; Gao, T.-N.; Fan, M.; Li, A.; Li, K.; Wang, T.; Huo, Q.; Qiao, Z.-A. A general ligand-assisted self-assembly approach to crystalline mesoporous metal oxides. *NPG Asia Materials* **2018**, *10* (8), 800-809. DOI: 10.1038/s41427-018-0072-z.
- (42) Lyu, W.; Liu, Y.; Chen, D.; Wang, F.; Li, Y. Engineering the electron localization of metal sites on nanosheets assembled periodic macropores for CO₂ photoreduction. *Nature Communications* **2024**, *15* (1), 10589. DOI: 10.1038/s41467-024-54988-3.
- (43) Xiao, S.; Wang, L.; Chen, L.; Li, Y.; Shen, K. Tandem Upgrading of Bio-Furans to Benzene, Toluene, and p-xylene by Pt₁Sn₁ Intermetallic Coupling Ordered Mesoporous SnO₂ Catalyst. *Advanced Materials* **2025**, *37* (4), 2415295. DOI: <https://doi.org/10.1002/adma.202415295>.
- (44) Liu, H.; Miao, B.; Chuai, H.; Chen, X.; Zhang, S.; Ma, X. Nanoporous tin oxides for efficient electrochemical CO₂ reduction to formate. *Green Chemical Engineering* **2022**, *3* (2), 138-145. DOI: <https://doi.org/10.1016/j.gce.2021.11.001>.
- (45) Ma, R.; Chen, Y.-L.; Shen, Y.; Wang, H.; Zhang, W.; Pang, S.-S.; Huang, J.; Han, Y.; Zhao, Y. Anodic SnO₂ porous nanostructures with rich grain boundaries for efficient CO₂ electroreduction to

- formate. *RSC Advances* **2020**, *10* (38), 22828-22835, 10.1039/D0RA03152F. DOI: 10.1039/D0RA03152F.
- (46) Bejtka, K.; Zeng, J.; Sacco, A.; Castellino, M.; Hernández, S.; Farkhondehfar, M. A.; Savino, U.; Ansaloni, S.; Pirri, C. F.; Chiodoni, A. Chainlike Mesoporous SnO₂ as a Well-Performing Catalyst for Electrochemical CO₂ Reduction. *ACS Applied Energy Materials* **2019**, *2* (5), 3081-3091. DOI: 10.1021/acsaem.8b02048.
- (47) Jiang, Y.; Shan, J.; Wang, P.; Huang, L.; Zheng, Y.; Qiao, S.-Z. Stabilizing Oxidation State of SnO₂ for Highly Selective CO₂ Electroreduction to Formate at Large Current Densities. *ACS Catalysis* **2023**, *13* (5), 3101-3108. DOI: 10.1021/acscatal.3c00123.
- (48) Ye, F.; Zhang, S.; Cheng, Q.; Long, Y.; Liu, D.; Paul, R.; Fang, Y.; Su, Y.; Qu, L.; Dai, L.; et al. The role of oxygen-vacancy in bifunctional indium oxyhydroxide catalysts for electrochemical coupling of biomass valorization with CO₂ conversion. *Nature Communications* **2023**, *14* (1), 2040. DOI: 10.1038/s41467-023-37679-3.
- (49) Yoon, Y.; Yan, B.; Surendranath, Y. Suppressing Ion Transfer Enables Versatile Measurements of Electrochemical Surface Area for Intrinsic Activity Comparisons. *Journal of the American Chemical Society* **2018**, *140* (7), 2397-2400. DOI: 10.1021/jacs.7b10966.
- (50) Brett, C. M. A. Electrochemical Impedance Spectroscopy in the Characterisation and Application of Modified Electrodes for Electrochemical Sensors and Biosensors. *Molecules* **2022**, *27* (5), 1497.
- (51) Lasia, A. Electrochemical Impedance Spectroscopy and its Applications. *Electrochemical Impedance Spectroscopy and its Applications* **2014**.
- (52) Wang, R.; Tao, J.; Du, K.; Wang, Y.; Ge, B.; Li, F.; Liu, W.; Wu, L.; Liu, H.; Zhang, Y.; et al. Transmission Electron Microscopy. In *Progress in Nanoscale Characterization and Manipulation*, Wang, R., Wang, C., Zhang, H., Tao, J., Bai, X. Eds.; Springer Singapore, 2018; pp 69-203.
- (53) Klein, N. D.; Hurley, K. R.; Feng, Z. V.; Haynes, C. L. Dark Field Transmission Electron Microscopy as a Tool for Identifying Inorganic Nanoparticles in Biological Matrices. *Analytical Chemistry* **2015**, *87* (8), 4356-4362. DOI: 10.1021/acs.analchem.5b00124.
- (54) Electron Spectroscopy. In *An Introduction to Surface Analysis by XPS and AES*, 2019; pp 1-18.

- (55) Sing, K. S. W. Reporting physisorption data for gas/solid systems with special reference to the determination of surface area and porosity (Recommendations 1984). *Pure and Applied Chemistry* **1985**, *57* (4), 603-619. DOI: doi:10.1351/pac198557040603.
- (56) Brunauer, S.; Emmett, P. H.; Teller, E. Adsorption of Gases in Multimolecular Layers. *Journal of the American Chemical Society* **1938**, *60* (2), 309-319. DOI: 10.1021/ja01269a023.
- (57) Thommes, M.; Kaneko, K.; Neimark, A. V.; Olivier, J. P.; Rodriguez-Reinoso, F.; Rouquerol, J.; Sing, K. S. W. Physisorption of gases, with special reference to the evaluation of surface area and pore size distribution (IUPAC Technical Report). *Pure and Applied Chemistry* **2015**, *87* (9-10), 1051-1069. DOI: doi:10.1515/pac-2014-1117.
- (58) Rahman, M. M.; Muttakin, M.; Pal, A.; Shafiullah, A. Z.; Saha, B. B. A Statistical Approach to Determine Optimal Models for IUPAC-Classified Adsorption Isotherms. *Energies* **2019**, *12* (23), 4565.
- (59) Heidary, N.; Ly, K. H.; Kornienko, N. Probing CO₂ Conversion Chemistry on Nanostructured Surfaces with Operando Vibrational Spectroscopy. *Nano Letters* **2019**, *19* (8), 4817-4826. DOI: 10.1021/acs.nanolett.9b01582.
- (60) Lin, L.; Bi, X.; Gu, Y.; Wang, F.; Ye, J. Surface-enhanced Raman scattering nanotags for bioimaging. *Journal of Applied Physics* **2021**, *129* (19). DOI: 10.1063/5.0047578.
- (61) Timoshenko, J.; Roldan Cuenya, B. In Situ/Operando Electrocatalyst Characterization by X-ray Absorption Spectroscopy. *Chemical Reviews* **2021**, *121* (2), 882-961. DOI: 10.1021/acs.chemrev.0c00396.
- (62) Timoshenko, J.; Jeon, H. S.; Sinev, I.; Haase, F. T.; Herzog, A.; Roldan Cuenya, B. Linking the evolution of catalytic properties and structural changes in copper–zinc nanocatalysts using operando EXAFS and neural-networks. *Chemical Science* **2020**, *11* (14), 3727-3736. DOI: 10.1039/D0SC00382D.
- (63) Mistry, H.; Varela, A. S.; Bonifacio, C. S.; Zegkinoglou, I.; Sinev, I.; Choi, Y.-W.; Kisslinger, K.; Stach, E. A.; Yang, J. C.; Strasser, P.; et al. Highly selective plasma-activated copper catalysts for carbon dioxide reduction to ethylene. *Nature Communications* **2016**, *7* (1), 12123. DOI: 10.1038/ncomms12123.

(64) Wang, J.; Hsu, C.-S.; Wu, T.-S.; Chan, T.-S.; Suen, N.-T.; Lee, J.-F.; Chen, H. M. In situ X-ray spectroscopies beyond conventional X-ray absorption spectroscopy on deciphering dynamic configuration of electrocatalysts. *Nature Communications* **2023**, *14* (1), 6576. DOI: 10.1038/s41467-023-42370-8.

Papers

The papers associated with this thesis have been removed for copyright reasons. For more details about these see:

<https://doi.org/10.3384/9789181186482>

FACULTY OF SCIENCE AND ENGINEERING

Linköping Studies in Science and Technology. Licentiate Thesis No. 2035, 2026
Department of Physics, Chemistry and Biology (IFM)

Linköping University
SE-581 83 Linköping, Sweden

www.liu.se